

Time propagation of extreme two-electron wavefunctions

F Robicieux

Department of Physics, Auburn University, AL 36849, USA

E-mail: robicfj@auburn.edu

Received 27 December 2011, in final form 18 May 2012

Published 19 June 2012

Online at stacks.iop.org/JPhysB/45/135007

Abstract

We develop a method for solving the time-dependent Schrödinger equation for the situation where two electrons interact in extreme circumstances. In particular, the method allows accurate representation of the wavefunction when several 10s or 100s of angular momenta are needed and the spatial region covers several 100s to 1000s of atomic units. The method is based on a discrete variable representation for the $\cos(\theta_{12})$ inside the $1/r_{12}$ operator. We also discuss a propagator for the radial part of the wavefunction which would allow efficient treatment of two continuum electrons as well as two Rydberg electrons. The method is tested on the case where two continuum electrons are successively launched from small r with zero angular momentum. The first electron has less energy so that the second electron must pass it. We show that the method is stable up to the highest angular momentum we tested: $\ell_{\max} = 160$. Although being a somewhat artificial case of post-collision interaction, this example has interesting features which we explore.

1. Introduction

One of the major successes in computational atomic and molecular physics is the treatment of quantum systems with two or three free electrons that interact in the continuum. Twenty years ago, this situation was intractable except when the electrons could be treated by perturbation theory. There are several methods that can now accurately compute total and differential cross sections in many situations. We cannot list all of the methods but we briefly describe a few of them to give an idea of the variety of computational techniques available. The time-dependent close-coupling method solves the time-dependent Schrödinger equation with the wavefunction projected onto continuum states to extract physically relevant parameters [1]. The convergent close-coupling method solves Green's function form of the time-independent Schrödinger equation using a basis set expansion [2]. The exterior complex scaling method solves the Schrödinger equation with the radius outside of a given distance rotated into the complex plane so that outgoing waves have only a finite spatial extent [3]. The R -matrix with pseudo-states uses the R -matrix method to obtain the scattering matrices using pseudo-states to represent the continuum electrons [4]. Except for a few cases, all of the methods agree quite well when applied to the same physical problem. The 'two-electron problem' has been declared 'solved' a few times.

It is a truism that all numerical methods have limitations so that, actually, it is not difficult to find situations where the methods above will not converge with current resources or would be so difficult to converge that it is not worth the effort. For example, Pisharody and Jones [5] describe an experiment where two electrons are launched in a wave packet so that both electrons are simultaneously in very highly excited states; to quantum mechanically represent this wavefunction, the spatial region would need to cover a few 1000 Bohr radii and could need individual angular momentum of $40\hbar$ or higher. This problem poses difficulties for the methods above because of the large spatial region and large number of angular momenta *and* because the amount of time needed for the simulation is $\sim 10^6$ atomic units. As another example, Landers *et al* [6] had a case of two continuum electrons where a slow electron is launched by photon absorption and then a much faster Auger electron is emitted from the ion which can interact with the slower electron during the escape; to quantum mechanically represent this wavefunction, the spatial region would need to cover several 100 Bohr radii, but the number of angular momenta needed for the wavefunction is not easy to estimate due to the extremely high energy of one of the electrons. This problem poses difficulties for the methods above because of the large spatial region and possibly large number of angular momenta *and* because the high energy of one of the electrons translates

to a very fine spatial grid or a large number of basis functions. Finally, Pisharody and Jones [7] describe an experiment which is a mixture of the two cases described above. In [7], two picosecond laser pulses were used to sequentially photoionize Ba so that two continuum electrons were produced. Since the second launched electron had higher energy than the first, it would have to pass the first electron and interact with it. The two laser pulse widths and central frequencies control the energies of the two electrons and their spatial and momentum width.

In this paper, we will describe an extension of the time-dependent close-coupling method that can be used to compute experimentally measurable parameters in the three situations described above. We will present detailed results for a difficult example case similar to [7] where two electrons are launched into the continuum by two separate laser pulses; in subsequent papers, we will treat the case with two continuum electrons like that reported in [6] as well as an example where the two electrons are launched into Rydberg wave packets as in [5]. Atomic units will be used unless explicitly stated otherwise.

2. Numerical method

In this section, we describe the particular numerical algorithms we have used to propagate the wavefunction. The most novel aspect of the propagation is the description of using the discrete variable method for the evaluation of the $1/r_{12}$ operator.

The method is directly applicable to Hamiltonians of the form

$$H = H_1 + H_2 + H_3, \quad (1)$$

where $H_i = p_i^2/2 + V(r_i, t)$ are the one-electron parts of the Hamiltonian and $H_3 = 1/r_{12}$. For example, the $V(r_i, t) = -2/r_i$ for the He atom. The time propagation can be used for both homogeneous and inhomogeneous Schrödinger's equations. An inhomogeneous Schrödinger equation can result when treating the photoionization of an atom or molecule [1]; the photon absorption can be incorporated by having a source term for the continuum wave with the form $(D_1 + D_2) \cos(\omega t) \Psi_g(t)$ where D_i are the dipole operators and Ψ_g is the ground-state wavefunction.

2.1. Time propagation

The present calculation has many elements used in other time-dependent methods. The method we used is most similar to that in [1] but with two important differences: (1) we use an implicit version of the split-operator technique instead of the leapfrog algorithm and (2) we evaluate the $1/r_{12}$ operator using a discrete variable technique [8–10] for the $\cos(\theta_{12})$ term instead of a multipole expansion.

For one time step, the unitary propagator is constructed using a split-operator technique of the form

$$U(\delta t) = U_1(\delta t/2)U_2(\delta t/2)U_3(\delta t)U_2(\delta t/2)U_1(\delta t/2), \quad (2)$$

where the unitary operators U_i can take many different forms. The form that will be used below is the implicit approximation:

$$U_j(\delta t) = \frac{1 - iH_j\delta t/2}{1 + iH_j\delta t/2} \quad (3)$$

which gives a single time step with order δt^3 accuracy; this implicit algorithm has been used for the TDCC method as applied to molecules [1]. Although we used this particular approximation, the methods described below would also work for other propagators (including the leapfrog algorithm, Chebyshev propagator, or the exponential method). The choice we make for the splitting means the U_1 and U_2 operators commute with each other. For computational efficiency, we do *not* use the simple application $U(2\delta t) = U(\delta t)U(\delta t)$; instead, we combine terms between the U_3 operators to make the replacement $U_1^2(\delta t/2) \rightarrow U_1(\delta t)$ and similarly for the U_2 operator.

We used the splitting where $H_3 = 1/r_{12}$ for the part of the Hamiltonian that couples the angular momenta of the electrons. The one-electron Hamiltonians $H_1 = p_1^2/2 - 2/r_1 - E_1$ and $H_2 = p_2^2/2 - 2/r_2 - E_2$ are shifted in energy so the time steps can be larger; the energies, E_1 and E_2 , are chosen to be relevant for the particular problem being modelled. The error in the propagator in equation (3) has the leading term $(H_j\delta t)^3/12$. If the wavefunction is peaked in energy, then subtracting the average energy from the Hamiltonian means the error in the propagator is related to the spread of energies in the packet. Thus, this shifting of the one-electron Hamiltonians allows time steps that are of order $\delta t \sim 0.1/\delta E$, where δE is the larger of the *spread* of energies for electron 1 or electron 2. Importantly, the implicit algorithm allows time steps to be more nearly related to the physical timescale of the problem instead of being related to the maximum angular momentum and/or the grid spacing as with an explicit method.

2.2. Discrete variable representation for $1/r_{12}$

As in equation (3) of [1], the wavefunction is represented by a superposition over coupled angular momenta with ℓ_1 and ℓ_2 coupled to total L and the spins coupled to total S ; we also represent the radial functions using a grid of points. As described in the next section, the action of the U_1 and U_2 operators on the wavefunction is easy to evaluate because the H_1 and H_2 operators are diagonal in ℓ and are taken to be tridiagonal in r .

The main difficulty we needed to overcome was the action of the U_3 operator on the wavefunction. We borrowed an idea from discrete variable representation to evaluate the action of U_3 [8]. We use our coupled angular momentum states as the orthonormal basis states $|i\rangle = |(\ell_{1i}, \ell_{2i})L\rangle$ and the $\cos(\theta_{12})$ operator as the coordinate. We can generate an orthonormal transformation matrix using the linear eigenvalue relations

$$\sum_j \chi_{ij} T_{j\alpha} = T_{i\alpha} \eta_\alpha, \quad (4)$$

where the $\chi_{ij} = \langle i | \cos(\theta_{12}) | j \rangle$ can be found in standard reference books [11]

$$\chi_{ij} = (-1)^{\ell_{2i} + \ell_{2j} + L} [l_{i1}, \ell_{i2}, l_{j1}, \ell_{j2}] \times \begin{pmatrix} \ell_{1i} & 1 & \ell_{1j} \\ 0 & 0 & 0 \end{pmatrix} \begin{pmatrix} \ell_{2i} & 1 & \ell_{2j} \\ 0 & 0 & 0 \end{pmatrix} \begin{Bmatrix} L & \ell_{2i} & \ell_{1i} \\ 1 & \ell_{1j} & \ell_{2j} \end{Bmatrix}, \quad (5)$$

where $[l_1, \ell_2, \dots] = \sqrt{(2\ell_1 + 1)(2\ell_2 + 1)\dots}$. When $L = 0$, the χ -matrix takes the particularly simple tridiagonal form: $\chi_{ij} = (\ell_i \delta_{\ell_i, \ell_j + 1} + \ell_j \delta_{\ell_i + 1, \ell_j}) / [\ell_i, \ell_j]$.

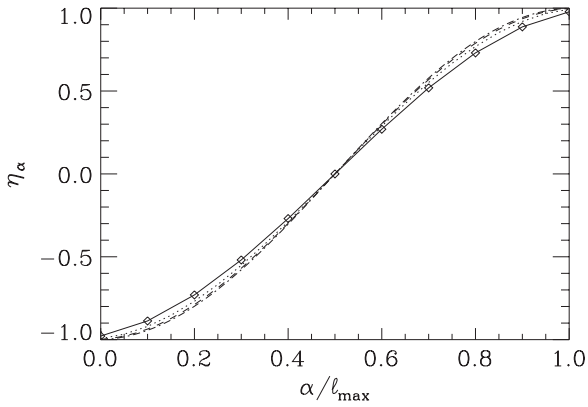


Figure 1. The eigenvalues η_α for $\ell_{\max} = 10$ (solid line and diamonds), 20 (dotted line), 40 (dashed line) and 80 (dash-dotted line). We have numbered the eigenvalues so that $\alpha = 0, 1, \dots, \ell_{\max}$.

The eigenvalues have the property $-1 < \eta_\alpha < 1$. If the wavefunction is represented as $\Psi(t) = \sum_i R_i(r_1, r_2, t)|i\rangle$, then the action of U_3 on $\Psi(t)$ changes the radial function as

$$R_i(r_1, r_2, t + \delta t) = \sum_{\alpha, j} T_{i\alpha} U_3(\eta_\alpha, \delta t) T_{j\alpha} R_j(r_1, r_2, t), \quad (6)$$

where the diagonal representation of U_3 can be written as

$$U_3(\eta_\alpha, \delta t) = \frac{2r_{12}(\eta_\alpha) - i\delta t}{2r_{12}(\eta_\alpha) + i\delta t} \quad (7)$$

with $r_{12}(\eta_\alpha) = \sqrt{r_1^2 + r_2^2 - 2r_1 r_2 \eta_\alpha}$. Because the eigenvalues η_α cannot equal ± 1 , the U_3 propagator is well defined and can be made to converge, for a fixed number of angular momentum channels, to the exact propagator as $\delta t \rightarrow 0$.

The early work on discrete variable representations [8] showed that the error resulting from truncating the number of states in the representation decreases faster than an inverse power of the number of states. This means that the practical convergence of this method is easily tested by increasing the number of states. Perhaps more importantly, all of the operations for applying the U_3 propagator to the wavefunction involve unitary transformations that are stable. Thus, we are able to solve for wavefunctions with $\ell > 100$ without degradation of the wavefunction due to numerical instabilities.

The eigenfunctions and eigenvalues have trends that can be understood in a general way. Figure 1 shows the eigenvalues for $L = 0$ when ℓ_{\max} is 10, 20, 40 and 80. For this figure, we have numbered the eigenvalues so that $\alpha = 0, 1, 2, \dots, \ell_{\max}$. These eigenvalues are approximately given by $\eta_\alpha \simeq \cos(\pi[2\ell_{\max} + 3/4 - \alpha]/[2\ell_{\max} + 3/2])$ which shows that the $\arccos(\eta_\alpha)$ are nearly equally spaced. Since the eigenvalues are within the fixed range $-1 < \eta_\alpha < 1$, the spacing gets finer with increasing ℓ_{\max} . Figure 2 shows the function that results from defining $F_\alpha(\cos(\theta_{12})) = \sum_i (\cos(\theta_{12})|i\rangle T_{i\alpha}$ for three eigenstates when $\ell_{\max} = 20$. It is clear that the resulting function is strongly peaked near the value where $\cos(\theta_{12}) \simeq \eta_\alpha$. The function becomes sharper as ℓ_{\max} increases and, in the limit $\ell_{\max} \rightarrow \infty$, the functions are only non-zero at the point $\cos(\theta_{12}) = \eta_\alpha$ and must be going to the square root of the delta function in order to be properly normalized. Finally, it is an interesting feature that the narrowest functions

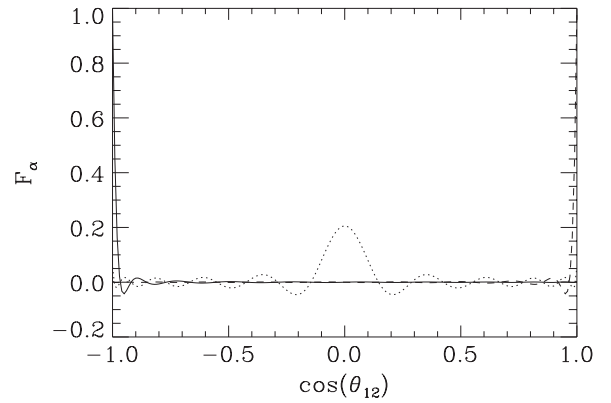


Figure 2. The function that results from using the eigenvectors to construct the corresponding eigenfunction in terms of $\cos(\theta_{12})$. This calculation is for $\ell_{\max} = 20$. The solid line represents the middle eigenvalue, $\eta_\alpha \simeq 0$, the dotted line represents the smallest eigenvalue, $\eta_\alpha \simeq -1$, and the dashed line represents the largest eigenvalue, $\eta_\alpha \simeq 1$. Note how the function is peaked near $\cos(\theta_{12}) = \eta_\alpha$.

are for the states corresponding to $\eta_\alpha \sim \pm 1$; this aids in the convergence of the wavefunction because the most spatially restricted functions cover the region where the $1/r_{12}$ operator most rapidly varies.

For a single r_1, r_2 point, the number of operations to compute the matrix element of the $1/r_{12}$ operator between all of the channels is CN_ℓ^2 where C is less than 10 and N_ℓ is the number of channels $|i\rangle = |(\ell_1, \ell_2)L\rangle$. If one keeps all of the terms in the multipole expansion of the $1/r_{12}$ operator, the number of operations scales like N_ℓ^3 . Restricting the terms in the multipole expansion (as described in [12]) reduces the number of operations to scaling like N_ℓ^2 times the number of multipoles; this approximation might not work so well when we want to focus on close interaction between two electrons that are simultaneously far from the nucleus. Other investigators have used a Schmidt decomposition of the $1/r_{12}$ operator (for example, see [13]); this decomposition will allow a fast computation of matrix elements between basis functions that include r_1, r_2 and angular functions. However, it was not clear to us whether this would work well for the extreme situations we are interested in.

2.3. Radial grid

We are interested in implementing this method for the case of two continuum electrons and for the case where one or both electrons are in Rydberg states. For grid methods, there can be a substantial gain in efficiency if the number of radial points per radial node remains roughly the same over the whole wavefunction. One way to estimate how the points should be positioned is to use equal steps in the phase, $\int p(r) dr$. Since $p(r) \propto 1/\sqrt{r}$ for small r and goes to a constant at large r , a good choice for the grid is a square root mesh at small r that smoothly transitions to a linear mesh at large r .

We have used the transformation

$$s = \sqrt{r}\sqrt{r_c + r} \quad \Leftrightarrow \quad r = \sqrt{\frac{r_c^2}{4} + s^2} - \frac{r_c}{2} \quad (8)$$

to define the variable s which we will use to specify the grid; the constant r_c roughly defines the distance where the grid transitions from being a square root mesh to a linear mesh and is chosen to be relevant for the particular problem. The radial grid will be equally spaced points in s where $s_j = \delta s j$. The spacing $\delta s = s_f/N$ is found from the final radial point r_f using $s_f = \sqrt{r_f}\sqrt{r_c + r_f}$ and the number of grid points N . The linear mesh results when $r_c = 0$ and the square root mesh results when $r_c \rightarrow \infty$.

We have implemented both a low-order and a higher order method for the action of the kinetic energy operator acting on the radial function. We will explain the different methods within the context of one-dimensional functions for simplicity; the extension to two-dimensional radial functions is straightforward. In what follows, $R_j = R(r_j)$ and similar constructions as appropriate.

The low-order method is similar to that in [14]. We make the substitution $R_j = y_j/\sqrt{r_{j+1} - r_{j-1}}$. This leads to the matrix expression

$$(Hy)_j = -\frac{y_{j+1}}{\Delta_j\sqrt{\lambda_j\lambda_{j+1}}} + \frac{y_j}{\Delta_j\Delta_{j-1}} - \frac{y_{j-1}}{\Delta_{j-1}\sqrt{\lambda_j\lambda_{j-1}}} + V_j y_j, \quad (9)$$

where $\Delta_j = r_{j+1} - r_j$ and $\lambda_j = r_{j+1} - r_{j-1} = \Delta_j + \Delta_{j-1}$. Equation (9) gives a symmetric tridiagonal representation of the H operator.

When solving the one-dimensional Schrödinger equation with a source term

$$i\frac{\partial R}{\partial t} - HR = S(t), \quad (10)$$

the approximation that goes with equation (3) is

$$y(t + \delta t) = \frac{1 - iH\delta t/2}{1 + iH\delta t/2}y(t) + \frac{-i\delta t}{1 + iH\delta t/2}\tilde{S}(t + \delta t/2), \quad (11)$$

where the source term $\tilde{S}_j(t) = \sqrt{\lambda_j}S(r_j, t)$ incorporates the rescaling of $R \rightarrow y$. This equation can be rearranged to the form

$$y(t + \delta t) = \Lambda(t) - y(t), \quad (12)$$

where the function $\Lambda(t)$ is the solution of the equation

$$(1 + iH\delta t/2)\Lambda = 2y(t) - i\delta t\tilde{S}(t + \delta t/2). \quad (13)$$

This is a tridiagonal matrix equation

$$a_j\Lambda_{j-1} + b_j\Lambda_j + c_j\Lambda_{j+1} = \sigma_j, \quad (14)$$

where $\sigma_j = 2y_j - i\delta t\tilde{S}_j$, $a_j = -i\delta t/(2\Delta_{j-1}\sqrt{\lambda_j\lambda_{j-1}})$, $b_j = 1 + i\delta t(V_j - E + 1/[\Delta_j\Delta_{j-1}])/2$ and $c_j = -i\delta t/(2\Delta_j\sqrt{\lambda_{j+1}\lambda_j})$. As we did above, we shift the Hamiltonian by the energy E so that we can take bigger time steps.

This propagator has several nice features. One of the important properties is that the norm is *exactly* conserved when $S = 0$. Because the operator of equation (9) is real and symmetric (thus, Hermitian), one can show that the propagator has the property that

$$\sum_j |y_j(t + \delta t)|^2 = \sum_j |y_j(t)|^2 \quad (15)$$

when $S = 0$. One can also show that $\langle H \rangle$ is a conserved quantity when H is time independent and $S = 0$. These two

properties mean that an eigenstate is propagated with only phase errors. The main negative feature of the propagator is that a low-order differencing scheme is used in equation (9). This means that the calculation will converge relatively slowly with the number of radial points.

To overcome the low-order spatial differencing, we can generalize the idea of a Numerov approximation to a nonlinear mesh. The appendix of [15] gave an expression for a Numerov approximation for a square root mesh. Robicheaux [15] started with the differential equation in terms of s . We will use a different approach.

The basic idea behind the Numerov approximation [16] is to start with a simple three-point difference and use a Taylor series expansion to express this difference in terms of second and higher derivatives of the function. For a differentiable function Ω , one can show that

$$\frac{2}{\lambda_j} \left(\frac{\Omega_{j+1} - \Omega_j}{\Delta_j} - \frac{\Omega_j - \Omega_{j-1}}{\Delta_{j-1}} \right) = \Omega_j'' + \frac{\Delta_j - \Delta_{j-1}}{3} \Omega_j''' + \frac{\Delta_j^3 + \Delta_{j-1}^3}{12\lambda_j} \Omega_j^{iv} + O(\Delta^4), \quad (16)$$

which reduces to the form of equation (9) if only the top line is kept. The order of the error is not obvious from this equation because the terms involving $\Delta_j - \Delta_{j-1}$ are actually proportional to δs^2 because they involve differences of the step in r . Next, use the differential equation for Ω to find expressions for the third- and fourth-order derivatives in terms of lower order derivatives. For example, if the differential equation is

$$\Omega''(r) = A(r)\Omega(r) + B(r), \quad (17)$$

then the substitutions

$$\Omega'''(r) = \frac{d}{dr} [A(r)\Omega(r) + B(r)] \quad (18)$$

and a similar expression for Ω^{iv} are useful. The first- and second-order derivatives can be approximated using three-point differences. This leads to the tridiagonal equation:

$$a_j\Omega_{j-1} + b_j\Omega_j + c_j\Omega_{j+1} = \alpha_j B_{j-1} + \beta_j B_j + \gamma_j B_{j+1}, \quad (19)$$

where

$$\begin{aligned} \alpha_j &= \frac{1}{6} - \frac{\Delta_j^2}{6\Delta_{j-1}(\Delta_j + \Delta_{j-1})} \\ \beta_j &= \frac{1}{2} + \frac{\Delta_j^2 + \Delta_{j-1}^2}{6\Delta_j\Delta_{j-1}} \\ \gamma_j &= \frac{1}{6} - \frac{\Delta_{j-1}^2}{6\Delta_j(\Delta_j + \Delta_{j-1})} \\ a_j &= \frac{2}{\Delta_{j-1}(\Delta_j + \Delta_{j-1})} - \alpha_j A_{j-1} \\ b_j &= -\frac{2}{\Delta_j\Delta_{j-1}} - \beta_j A_j \\ c_j &= \frac{2}{\Delta_j(\Delta_j + \Delta_{j-1})} - \gamma_j A_{j+1} \end{aligned} \quad (20)$$

result from taking the appropriate three-point differences for the first and second derivatives of the combination $A(r)\Omega(r) + B(r)$. This expression reduces the error by a factor of δs^2 from the simple three-point scheme in equation (9).

To implement the Numerov approximation, we note that the propagator leads to the relation

$$R(t + \delta t) = \frac{1 - iH\delta t/2}{1 + iH\delta t/2}R(t) = \Omega(t) - R(t), \quad (21)$$

where the $\Omega(t)$ function is the solution of

$$(1 + iH\delta t/2)\Omega(t) = 2R(t). \quad (22)$$

We can identify the parameters in equation (20) for the grids in r_1 and r_2 as being

$$A_j = 2(V_j - E) - \frac{4i}{\delta t} \quad \text{and} \quad B_j = \frac{8i}{\delta t}R_j, \quad (23)$$

where the grid and the energy, E , are appropriate for the direction r_1 or r_2 . We used the expression

$$\langle R|R \rangle = \sum_j \frac{s_j}{\sqrt{s_j^2 + r_c^2/4}} |R_j|^2 \delta s \quad (24)$$

to compute the norm of the wavefunction (and similar expressions for the expectation values).

Although the Numerov method above gives faster convergence with the number of radial points, we lose an important feature of the simple three-point method: exact norm conservation. The tridiagonal equations we solve with the Numerov method do not have exactly symmetrical Hamiltonians. We found that there *was* a small change in the norm. However, the change was not an exponential increase or decrease. The change seemed to depend on where the wave packet was centered and, thus, there seems to be a slight problem with how the definition of the norm was chosen. Interestingly, a pure linear mesh ($r = s$) or pure square root mesh ($r = \sqrt{s}$) seemed to have perfect norm conservation. The error in the norm decreased like δs^4 so that changing the number of radial mesh points allows a simple test of whether the norm problem affects the final results; the change in norm was at the couple parts per 10^5 for the cases presented below.

Figure 3 shows a comparison of the convergence with respect to the number of points for the simple three-point approximation (figure 3(a)) and the Numerov approximation (figure 3(b)). In this case, we start an $E = 1$ au packet at $r = 200$ au with a spatial width of 40 au with a negative radial velocity. The potential was chosen to be $-1/r$ and $\ell = 0$. We propagated the packet for 300 au of time and the plot shows the $|R|^2$ at the final time. We used a grid with $r_c = 5$ au. As can be seen from figure 3(a), there is a qualitative error for 400 points. There is a substantial error for 800 points as well; the error in the group velocity is $\sim 8\%$. While 1600 points give a reasonable accuracy ($\sim 3\%$ error in group velocity), it is only when using 3200 points that the error in the one-dimensional calculation drops below 1%. In contrast, the Numerov approximation (figure 3(b)) is more accurate for 400 points ($\sim 6\%$ error in group velocity) than the simple three-point approximation was for 800 points. Also, the higher power of convergence means that 800 points for the Numerov approximation gives errors much less than 1% in the group velocity.

The Numerov approximation requires only slightly more operations than the simple three-point method. The two methods require approximately the same CPU time when using the same number of points because the only difference in

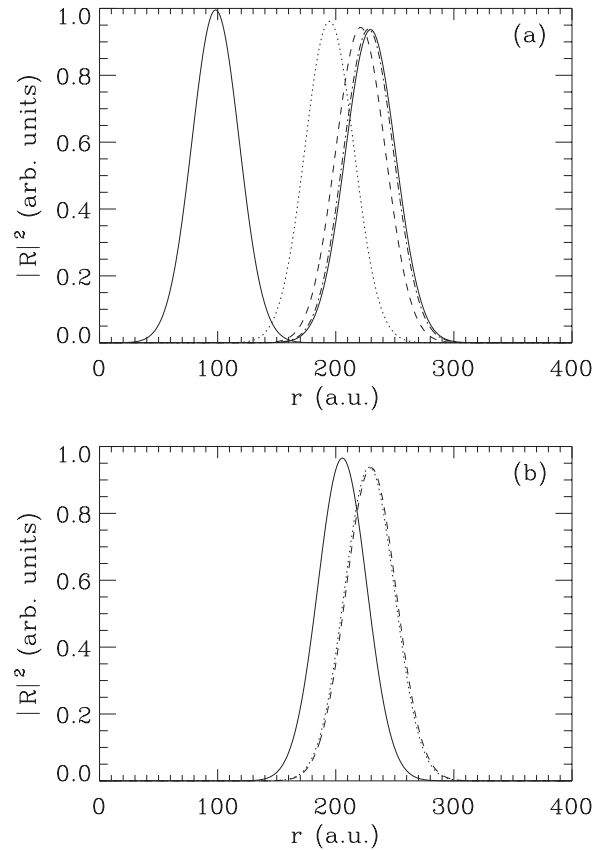


Figure 3. Convergence of the radial probability at the final time as a function of the number of grid points. (a) The simple three-point differencing scheme with 400 (solid line), 800 (dotted line), 1600 (dashed line), 3200 (dash-dotted line) and 6400 (dash-dot-dot-dotted line) points. (b) The Numerov approximation using 400 (solid line), 800 (dotted line) and 1600 (dashed line) points.

computational time is due to the right-hand side of equation (19) having two more multiplications and additions than the right-hand side of equation (14); these extra operations are a small fraction of the total number of operations which means that the additional computational load for the Numerov method is small. The difference between the convergence of the two methods is important because there are two radial coordinates. Thus, if we can use two times fewer points in each direction, we can obtain a factor of 4 speedup in the calculation.

In the results presented below, we used the Numerov approximation exclusively. We have performed calculations with both methods for some test cases and found that the converged results of each method agreed well with each other.

3. Example problem

In this section, we present results from an example case where two electrons are successively launched from a neutral atom. Pisharody and Jones [7] investigated the effect of energy transfer between the two electrons successively launched from Ba. Their measurement of the energy transfer agreed well with classical calculations and a quantum ‘sudden’ approximation. We find that our quantum calculations are accurately reproduced by a classical calculation for the energy

transfer between electrons. We will also investigate the angular correlation of the electrons where the agreement between classical and quantum calculations is only qualitative at best.

We will first launch a slow electron $E = 4$ eV and then a faster electron (energies of 1, 2, or 4 au). We will launch both electrons as s-waves so that the total wavefunction has $L = 0$; this condition is not necessary but does simplify the calculation. The second electron passes the first electron and can strongly interact with it if they are launched with similar angles. Thus, a situation similar to that in [6] is obtained but where the characteristics of the second electron are controlled.

As with [6], one of the main quantities of interest is the energy distributions of the two electrons after the second electron passes the first. Another quantity of interest is the distribution of the wavefunction with respect to $\cos(\theta_{12})$. Because the electrons will only pass each other at large r , the wavefunction has almost no dependence on $\cos(\theta_{12})$ except where it is approximately 1. For $\cos(\theta_{12}) \sim 1$, there will be less probability because the electrons repel each other.

The intensity of the source that launches the electron will have a time width of $t_{w,1} = 40$ au FWHM which will correspond to a FWHM spread in energy $\delta E = 4 \ln 2 / t_{w,1} \simeq 0.069$ au (~ 1.9 eV) around the central energy of 0.147 au (~ 4 eV). For all of the cases, we will delay the launch of the second electron by 120 au. Finally, all of the calculations will take place within a region $r_{1,2} \leq 400$ au. The grid for electron 1 will have $r_c = 20$ au and for electron 2 will have $r_c = 5$ au. We will not symmetrize the wavefunction because the disparate energies of the two electrons mean that there is no overlap in energy space; the lack of overlap means that the singlet and triplet wavefunctions will give the same results. Finally, we used 400 grid points for r_1 direction in all of the calculations.

3.1. Quantum theory

The successive launch of two electrons is computed by casting this problem as two perturbative interactions that start the electrons near the nucleus with positive energy; the process that launches the electrons is considered as perturbative but the electron–electron interaction is *not* treated perturbatively.

When the first electron is launched, there is only one active electron. Thus, for the first electron, we solve the first order time-dependent perturbation equation:

$$i \frac{\partial R_1(r_1, t)}{\partial t} - (H_0 - E_1)R_1(r_1, t) = S_1(r_1)G_1(t), \quad (25)$$

where E_1 is the central energy of electron 1 after it is fully launched, R_1 is the radial part of the wavefunction for $\ell = 0$, the potential in H_0 is $-1/r$, $S_1(r_1)$ is any radial function with a small radial extent (less than a couple atomic units) and *not* orthogonal to the continuum waves at energy E_1 and $G_1(t) = \exp(-2 \ln 2 t^2 / t_{w,1}^2)$; $t_{w,1}$ is the FWHM of the time width of the electron's launch. For times larger than a few $t_{w,1}$, the time-dependent function $R_1(r_1, t)$ gives an outgoing radial wave packet with energy centered at E_1 . The energy distribution of the wave packet is a Gaussian with a FWHM of $\delta E = 4 \ln 2 / t_{w,1}$. We start the time propagation at a time $-t_{w,1} \sqrt{15 / \ln 2}$ which is early enough that the source term, $S_1(r_1)G_1(t)$, is effectively 0.

The launch of the second electron is accomplished by solving the inhomogeneous Schrödinger equation:

$$i \frac{\partial \Psi(t)}{\partial t} - (H - E_1 - E_2)\Psi(t) = R_1(r_1, t)S_2(r_2)G_2(t), \quad (26)$$

where E_2 is the central energy of electron 2 after it is fully launched, $\Psi(t)$ is the full two-electron wavefunction, the potential in the Hamiltonian is the full $-2/r_1 - 2/r_2 + 1/r_{12}$, $S_2(r_2)$ is any radial function with a small radial extent (less than a couple atomic units), and $G_2(t) = \exp(-2 \ln 2 (t - t_d)^2 / t_{w,2}^2)$; $t_{w,2}$ is the FWHM of the time width of the second electron's launch and t_d is the delay between the launches. This form for the source does not include an effect of the presence of electron 1 in the continuum on the absorption of the second photon by electron 2; this should be an excellent approximation since electron 1 has a wave packet that is localized more than 70 au from the nucleus when the second electron absorbs its photon. For times larger than a few $t_{w,2}$ after the delay t_d , the wavefunction Ψ gives two outgoing electrons with electron 1 centered at energy E_1 and electron 2 centered at E_2 . In all cases below, we have chosen the delay $t_d = 120$ au which gives electron 1 time to reach ~ 100 au before the electrons pass each other.

We note that the time dependence of each of the source terms, $G_1(t)$ and $G_2(t)$, is a real Gaussian. We have made this choice so that the electron launch is not chirped. If a chirp is desired, then the right-hand side is modified by multiplying by a factor like $\exp(it^2 / \tau^2)$.

3.2. Classical theory

The situation described in the previous section has a classical analogue which we can explore using a classical trajectory Monte Carlo calculation. It is interesting to perform a classical calculation that most nearly matches the quantum conditions. We can then compare several aspects of the classical and the quantum calculations to obtain insight into how well the classical calculation approximates the actual results.

In the classical calculation, we made a small change to the Coulomb potential in order to make the calculations slightly more tractable. Instead of using $1/r$, we used $1/\sqrt{r^2 + a^2}$ for all of the Coulomb interactions. We used $a = 0.001$ au. This does not change the results in an appreciable manner because the energy scale associated with $1/a$ is more than a factor of 100 larger than the energies in the calculation.

We performed the calculation in two steps to match the quantum treatment. Electron 1 was launched from $r = 0$ with a random time chosen from a distribution $\exp(-4 \ln 2 t^2 / t_{w,1}^2)$, with a random energy chosen from a distribution $\exp(-4 \ln 2 [E - E_1]^2 / \delta E_1^2)$ where $\delta E_1 = 4 \ln 2 / t_{w,1}$, and with a random direction for the radial velocity chosen from flat $\cos(\theta)$ and flat ϕ distributions. Until electron 2 is launched, electron 1 only experiences the potential $-1/\sqrt{r_1^2 + a^2}$. If electron 1 is chosen to have energy E , then its speed at $r = 0$ is given by $v = \sqrt{2(E + 1/a)}$.

Electron 2 was also launched from $r = 0$ but with a random time chosen from a distribution $\exp(-4 \ln 2 (t - t_d)^2/t_{w,2}^2)$ which guarantees that it is launched after the first electron. Electron 2 is launched with a random energy chosen from a distribution $\exp(-4 \ln 2 [E - E_2]^2/\delta E_2^2)$, where $\delta E_2 = 4 \ln 2/t_{w,2}$ and with a random direction for the radial velocity chosen from flat $\cos(\theta)$ and flat ϕ distributions. After electron 2 is launched, the electrons' motion are computed using the potential $-2/\sqrt{r_1^2 + a^2} - 2/\sqrt{r_2^2 + a^2} + 1/\sqrt{r_{12}^2 + a^2}$. If electron 2 is chosen to have energy E , then its speed at $r = 0$ is given by $v = \sqrt{2(E + 2/a)}$. We run the classical simulation to the same final time as the quantum calculation so that we can compare the results as closely as possible.

3.3. Quantum results

We performed calculations for three different values of E_2 : 1, 2 and 4 au. The three different calculations used somewhat different parameters for the width and the grid. Also, since the fast electron's speed changes by a factor of 2, the total time for the calculations varied with E_2 . The next paragraph gives parameters used in the three different calculations with the ordering of the parameters always for $E_2 = 1, 2$ and 4 au. As a test, we also performed a calculation slightly modifying an existing leapfrog TDCC code [1] for $E_2 = 1$ au and obtained perfect agreement when the calculations were converged.

We chose the width of the second electron's launch, $t_{w,2}$, to be 15, 10 and 7 au for the cases of $E_2 = 1, 2$ and 4 au, respectively. Thus, the largest energy spread is from the second electron which has a FWHM $\simeq 0.18, 0.28$ and 0.40 au, respectively. Thus, we expect time steps of $\sim 1, 0.7$ and 0.5 au to give converged results; the error in the implicit time propagator will be of size $\sim (\delta E \delta t)^3/12$ which is $\sim 1/2000$ for all cases. We tested this assumption by comparing the $\ell_{\max} = 10$ and the $\ell_{\max} = 80$ calculations to those performed with the δt decreased by a factor of 2 and found the change to be less than 1%. The results presented below used 800, 1200 and 1600 mesh points, respectively, for electron 2; we performed a test calculation for $\ell_{\max} = 10$ using $2\times$ more mesh points for both r_1 and r_2 and found the results changed by less than 1%. We propagated the wavefunction to a final time of 240, 170 and 120 au after the launch of the second electron (i.e. until $t = 360, 290$ and 240 au). We found that there was some reflection from the box at $r = 400$ au at the latest times so that the results presented below are actually at the time 216.5, 162.75 and 115.25 au after the launch of the second electron.

The most difficult aspect of this problem to converge is the angular correlation. For most of $\cos(\theta_{12})$, the distribution is flat. Only in a small region near $\cos(\theta_{12}) = 1$ is the distribution not flat; this is the region that most sensitively tests the electron-electron interaction. We have computed two different $\cos(\theta_{12})$ distributions. The uppermost curve in figure 4 shows the distribution obtained by integrating over r_1 and r_2 :

$$D_r(\cos(\theta_{12})) \equiv \int |\Psi(r_1, r_2, \cos(\theta_{12}))|^2 dr_1 dr_2 \quad (27)$$

which reflects the angular distribution at the time 216.5 au after the launch of the second electron. The curves on figure 4 show the angular distribution for half of the range of $\cos(\theta_{12})$ when

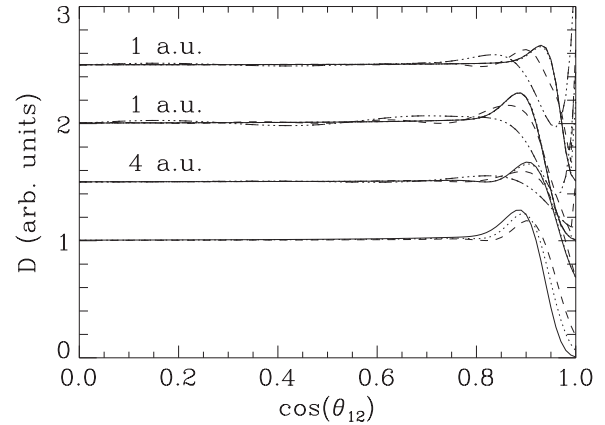


Figure 4. The top set of curves (shifted up by 1.5) are the spatial angular distribution (integrating over r_1 and r_2) for the case when $E_2 = 1$ au for different ℓ_{\max} : $\ell_{\max} = 10$ (dash-dot-dotted line), 20 (dashed line), 40 (dotted line), 80 (solid line) and 160 (dash-dotted line). The $\ell_{\max} = 160$ line is indistinguishable from that for $\ell_{\max} = 80$. The next set of curves (shifted up by 1.0) give the momentum space angular distribution (integrating over k_1 and k_2) for the case when $E_2 = 1$ au for different ℓ_{\max} . The next set of curves (shifted up by 0.5) give the momentum space angular distribution for the case when $E_2 = 4$ au for different ℓ_{\max} . The bottom set of curves compare the converged momentum space angular distribution for $E_2 = 1$ au (solid line), for $E_2 = 2$ au (solid line) and for $E_2 = 4$ au (dashed line).

the calculation has an $\ell_{\max} = 10, 20, 40, 80$ and 160. These curves were plotted with a step of 0.01 and are normalized by the same factor so that the result for $\ell_{\max} = 160$ at $\cos(\theta_{12}) = -1$ exactly equals 1.

Figure 4 has a similar property to that seen in [6] although the double launch substantially differs from the Auger process in [6]. The distribution is essentially flat except near 1. The region near $\cos(\theta_{12}) = 1$ represents the case where electron 2 has nearly the same ejection angle as electron 1. As electron 2 passes through the electron 1 wavefunction, the repelling $1/r_{12}$ interaction causes the hole in the distribution. The part of the electron distribution near $\cos(\theta_{12}) = 1$ is pushed to larger angles (smaller $\cos(\theta_{12})$) and leads to the peak near 0.93.

As can be seen, the $\ell_{\max} = 80$ result is indistinguishable from the 160 result on this graph (the largest difference was less than 0.002); the $\ell_{\max} = 40$ curve is converged except for the point at 1. At $\cos(\theta_{12}) = 1.00$, the $\ell_{\max} = 160$ result is 0.0084, the 80 result is 0.0102, the 40 result is 0.69, the 20 result is 1.16 and the 10 result is 1.90. At $\cos(\theta_{12}) = 0.99$, the 160 result is 0.0695, the 80 result is 0.0695, the 40 result is 0.0700, the 20 result is 0.18 and the 10 result is 1.2.

The uppermost curves in figure 4 reflect the spatial distribution at the final time. Pindzola *et al* [1] show how to project the wavefunction onto Coulomb waves to extract a better approximation to the $t \rightarrow \infty$ angular distribution. The only feature we changed was to project onto continuum waves with a $-2/r$ potential for electron 1 and a $-1/r$ potential for electron 2. The next lower curves in figure 4 show the distribution using the momentum-space angular distribution; it shows a shape similar to the upper curves but the region of the hole is bigger. This reflects the fact that as time increases, there is more opportunity for the momentum transferred from

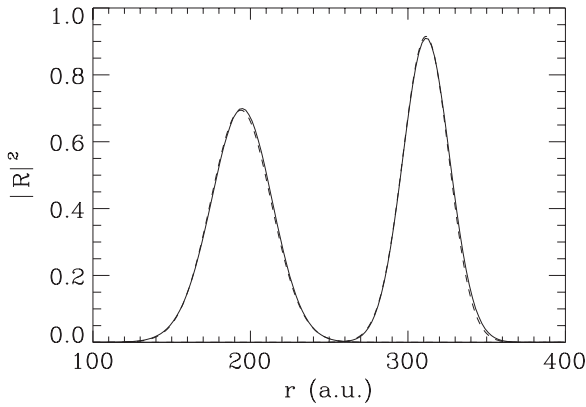


Figure 5. Comparison between the quantum (dashed line) and classical (solid line) radial distributions for electron 1 (packet centered near 190 au) and for electron 2 (packet centered near 310 au) for the case where $E_2 = 1$ au.

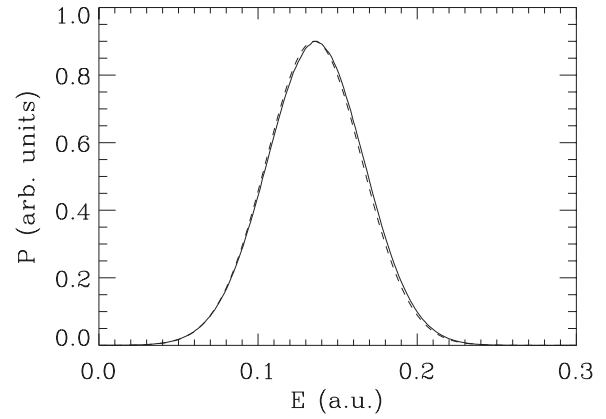


Figure 6. Comparison between the quantum (dashed line) and classical (solid line) energy distribution for electron 1 for the case where $E_2 = 4$ au. The approximately 0.011 au energy shift from the initial distribution centered at 0.147 au is due to post-collision interaction.

electron 2 to electron 1 to cause the angular separation of the electrons to increase. The converged value at $\cos(\theta_{12}) = 1$ is 0.0071.

The next lower curves on figure 4 show the angular distribution after projecting onto the continuum waves for $E_2 = 4$ au; we did not include an $\ell_{\max} = 160$ calculation for this energy. The shape is similar to the momentum distribution for $E_2 = 1$ au but the peak is not as high nor is the hole as deep.

The lowest curves on figure 4 compare the converged angular distributions in momentum space for $E_2 = 1, 2$ and 4 au. As the energy increases, the depth of the hole at $\cos(\theta_{12}) = 1$ decreases. The $\cos(\theta_{12}) = 1$ is 0.0071 for $E_2 = 1$ au but is 0.061 for $E_2 = 2$ au and is 0.19 for $E_2 = 4$ au. Another feature is that the height of the peak decreases and its position moves closer to $\cos(\theta_{12}) = 1$ with increasing energy. Another feature is that there is a slight dip in the distribution for $E_2 = 4$ au near 0.82.

These three calculations (for $E_2 = 1, 2$ and 4 au) show that this method for propagating the wavefunction can give stable converged results even for very large ℓ_{\max} . Although $\ell_{\max} = 160$ was not necessary, it was heartening to find that no problems developed at large ℓ_{\max} . If a standard multipole expansion for the $1/r_{12}$ operator is used in a calculation with $\ell_{\max} = 160$, then up to the 320th multipole would have a non-zero contribution to the interaction.

3.4. Quantum/classical comparison

In this section, we compare quantum and classical distributions to gain insight into the fully quantum calculation. For consistency, we will use quantum calculations with $\ell_{\max} = 80$ unless specifically stated otherwise.

Figure 5 shows the radial distribution of electrons 1 and 2 for the case $E_2 = 1$ au. The two classical distributions are represented by the solid lines and the quantum distributions are represented by the dashed lines. For the quantum calculation, the radial distribution is obtained by integrating the squared magnitude of the wavefunction over the other radial coordinate

and summing over ℓ . There is remarkably good agreement between the classical and quantum results. There is a slight difference: the classical distribution is at slightly larger r . This difference is partly due to the slight inaccuracy in the group velocity (see figure 3(b)). Also, this difference might be due to how the source term was implemented in the split-operator method; the order of operations might lead to an artificial time shift of order $\delta t/2$.

Figure 6 shows the energy distribution of electron 1 for the case $E_2 = 4$ au. Just as in the previous figure, the agreement is very good. Both have a distribution shifted to lower energy by 0.011 au compared to the initial energy distribution which is centered at 0.147 au. The shift in energy is the well-known effect that arises due to the effective potential for electron 1 changing from $-1/r$ to $-2/r$ as electron 2 passes it. As with figure 5, there is a slight shift in the distribution, but the shift is much smaller than the other energy scales.

Figure 7 shows three different angular distributions. These distributions illustrate a distinct difference between the quantum and classical calculations. For these plots, we normalized the curves so that the sum of the values equals the number of points. In these three sets of curves, the background values match incredibly well which indicates the integral over the distribution near $\cos(\theta_{12}) = 1$ must be very similar for the quantum and classical distributions. The lowest curves are for $E_2 = 1$ au and shows the angular part of the spatial distribution (see figure 4, uppermost curves). Although similar results are obtained, the classical calculation gives a sharper structure and the distribution exactly goes to 0 at $\cos(\theta_{12}) = 1$. The upper two pairs of curves include the approximate contribution obtained by projecting on the continuum states for $E_2 = 1$ and 4 au (see figure 4, lower curves). The differences between the classical and quantum calculations are even more pronounced. Again, the classical calculations give a much narrower feature in the angular distribution and the classical calculation goes exactly to 0 at $\cos(\theta_{12}) = 1$.

It is easy to understand why the classical calculations behave as they do. As the energy for electron 2 increases, the

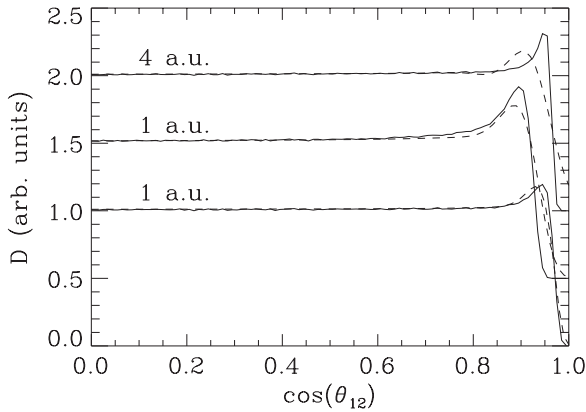


Figure 7. The bottom curves compare the quantum (dashed line) and classical (solid line) spatial angular distribution (see figure 4) for the case where $E_2 = 1$ au. The next curves (shifted up by 0.5) compare the quantum (dashed line) and classical (solid line) momentum space angular distribution for the case where $E_2 = 1$ au. The top curves (shifted up by 1.0) compare the quantum (dashed line) and classical (solid line) momentum space angular distribution for the case where $E_2 = 4$ au.

momentum transfer to electron 1 will be less. This will lead to a smaller region where the electrons strongly interact; this leads to the narrowing of the feature in the classical distribution when going from $E_2 = 1$ –4 au. Also, the classical distribution must go to 0 at $\cos(\theta_{12}) = 1$ because the repelling $1/r_{12}$ interaction only moves electrons from this region. In [6], the Auger electron has ~ 30 au of energy. From figure 7, it is perhaps understandable that the classical calculation in [6] gave poor results since the trend is that the higher energy E_2 gives less agreement between classical and quantum calculations.

The peak of the quantum distribution does move to larger $\cos(\theta_{12})$ but the effect is not as striking as in the classical calculation. Also, the quantum distribution is not 0 at $\cos(\theta_{12}) = 1$ and gets larger with increasing E_2 . This behaviour is being controlled by the competition between the repelling $1/r_{12}$ interaction and the diffraction of the electron waves around small features in the potential. The effective distance of closest approach of the two electrons scales like $1/E_2$ so increasing this energy will lead to a relatively larger amount of diffraction.

Another way of interpreting this result is by examining the angular momentum distribution at the final time. Figure 8 shows the quantum (lines) and classical (symbols) results for $E_2 = 1, 2$ and 4 au. For the classical calculation, the probability to be in angular momentum ℓ was taken to be the probability for electron 1 (or electron 2 since $L = 0$) to have angular momentum between ℓ and $\ell + 1$. Remarkably, the classical and quantum results track each other quite well over several orders of magnitude. The exception is for $E_2 = 2$ au for $\ell > 76$ which is due to the fact that the quantum calculations have $\ell_{\max} = 80$. It is important to realize that features in the quantum angular distributions, figures 4 and 7, must arise from superposing Legendre polynomials. To obtain a sharp feature in $\cos(\theta_{12})$, many angular momenta must add up coherently. As E_2 increases, the angular momentum distribution decreases

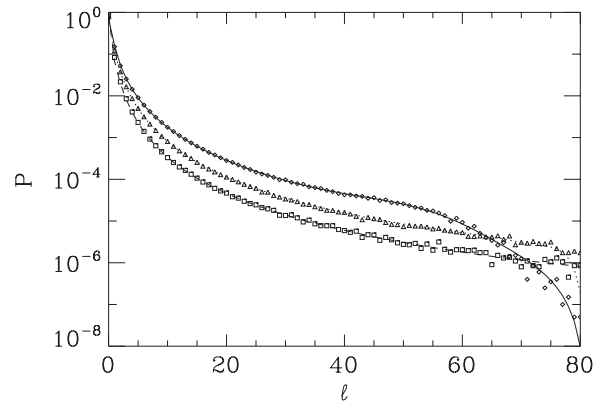


Figure 8. Comparison between the quantum (lines) and classical (symbols) angular momentum distributions for the cases $E_2 = 1$ au (solid line and diamonds), 2 au (dotted line and triangles) and 4 au (dashed line and squares). The $E_2 = 1$ and 2 au has $\ell_{\max} = 80$ which leads to an unphysical extreme drop for ℓ above 76. The $E_2 = 4$ au has $\ell_{\max} = 160$. The rapid drop of the $E_2 = 1$ au result starting at $\ell \sim 60$ is physical and is due to a classical condition on the maximum angular momentum that can be transferred during the scattering.

more quickly with ℓ which leads to the broader feature in $\cos(\theta_{12})$.

There is one last physical property of interest in figure 8. The angular momentum distribution for $E_2 = 1$ au is larger than for the $E_2 = 2$ or 4 au cases until $\ell \sim 60$ after which point there is a sharp drop in both the quantum and classical calculations for $E_2 = 1$ au. This can be understood from a qualitative classical argument. The collision of the two electrons takes place when they are far from the nucleus. This means that we can estimate the maximum angular momentum after the collision from a collision of two free electrons. The largest perpendicular speed after the collision is $v_2/2$ in a collision of free electrons where $v_1 \ll v_2$. This leads to an estimated maximum ℓ of $r_{\text{col}}\sqrt{E_2/2}$. Since the collision takes place near $r_{\text{col}} \sim 100$ au this leads to a maximum angular momentum of ~ 70 au for $E_2 = 1$ au. There is a very sharp drop in the distribution near this value which is also produced in the $\ell_{\max} = 160$ quantum calculation. The angular momenta distributions for $E_2 = 2$ and 4 au extend to higher ℓ .

4. Conclusions

We performed fully quantum calculations for the situation where a slow photoelectron interacts with a much higher energy electron that was launched after it. We presented a treatment of the time propagation of the two-electron wavefunction which used a discrete variable representation of the $\cos(\theta_{12})$ inside of the $1/r_{12}$ operator which allowed us to stably propagate wavefunctions with $\ell_{\max} = 160$. We showed that important parameters from the two-electron wavefunction could be converged with errors less than 1%.

In our application of this method to a model problem similar to the experiment [7] involving a sequential two-electron launch, we showed how the angular distribution evolved with increasing energy of the second electron. We also

compared our results to a classical model and showed that only the angular distribution showed a substantial disagreement between the classical and quantum calculations. We argued that the disagreement in the angular distribution is due to the fast decrease in the population as a function of ℓ .

All of the calculations presented in this paper were performed on a single processor machine with less than 2 Gb of RAM. It seems like an implementation on a parallel computer would allow treatment of more complicated two-electron interactions. We have already implemented this method for the situations corresponding to the experiments described in [5] and [6]. We think that it might be possible to also use this method to extend the calculations of electron–atom scattering to the case where the atom is in more highly excited Rydberg states than those treated in [17].

Acknowledgments

This work was made possible in part by a grant of high performance computing resources and technical support from the Alabama Supercomputer Authority. This work was supported by the Chemical Sciences, Geosciences, and Biosciences Division of the Office of Basic Energy Sciences, US Department of Energy.

References

- [1] Pindzola M S *et al* 2007 *J. Phys. B: At. Mol. Opt. Phys.* **40** R39
- [2] Bray I and Fursa D V 1996 *Phys. Rev. Lett.* **76** 2674
- [3] McCurdy C W, Baertschy M and Rescigno T N 2004 *J. Phys. B: At. Mol. Opt. Phys.* **37** R137
- [4] Bartschat K *et al* 1996 *J. Phys. B: At. Mol. Opt. Phys.* **29** 115
- [5] Pisharody S N and Jones R R 2004 *Science* **303** 813
- [6] Landers A L *et al* 2009 *Phys. Rev. Lett.* **102** 223001
- [7] Pisharody S N and Jones R R 2003 *Phys. Rev. Lett.* **91** 203002
- [8] Harris D O, Engerholm G G and Gwinn W D 1965 *J. Chem. Phys.* **43** 1515
- [9] Dickinson A S and Certain P R 1968 *J. Chem. Phys.* **49** 4209
- [10] Light J C and Carrington T Jr 2000 *Adv. Chem. Phys.* **114** 263
- [11] Edmonds A R 1960 *Angular Momentum in Quantum Mechanics* (Princeton, NJ: Princeton University Press)
- [12] Taylor K T *et al* 2004 *Phys. Scr. T* **110** 154
- [13] Jordan G, Caillat J, Ede C and Scrinzi A 2006 *J. Phys. B: At. Mol. Opt. Phys.* **39** S341
- [14] Witthoef M C, Pindzola M S and Colgan J 2003 *Phys. Rev. A* **67** 032713
- [15] Robicheaux F 1996 *J. Phys. B: At. Mol. Opt. Phys.* **29** 779
- [16] Koonin S E and Meredith D C 1986 *Computational Physics* (Menlo Park, CA: Benjamin/Cummings)
- [17] Griffin D C, Ballance C P, Pindzola M S, Robicheaux F, Loch S D, Ludlow J A, Witthoef M C, Colgan J, Fontes C J and Schultz D R 2005 *J. Phys. B: At. Mol. Opt. Phys.* **38** L199